Automated white corpuscles nucleus segmentation using deep neural network from microscopic blood smear

Indrajeet Kumar[a,*], Chandradeep Bhatt[a], Vrince Vimal[a] and Shamimul Qamar[b]
[a]*Graphic Era Hill University, CSE Department, Dehradun, India*
[b]*College of Science and Arts Dhahran Al Janub King Khalid University ABHA, Saudi Arabia*

Abstract. The white corpuscles nucleus segmentation from microscopic blood images is major steps to diagnose blood-related diseases. The perfect and speedy segmentation system assists the hematologists to identify the diseases and take appropriate decision for better treatment. Therefore, fully automated white corpuscles nucleus segmentation model using deep convolution neural network, is proposed in the present study. The proposed model uses the combination of 'binary_cross_entropy' and 'adam' for maintaining learning rate in each network weight. To validate the potential and capability of the above proposed solution, ALL-IDB2 dataset is used. The complete set of images is partitioned into training and testing set and tedious experimentations have been performed. The best performing model is selected and the obtained training and testing accuracy of best performing model is reported as 98.69 % and 99.02 %, respectively. The staging analysis of proposed model is evaluated using sensitivity, specificity, Jaccard index, dice coefficient, accuracy and structure similarity index. The capability of proposed model is compared with performance of the region-based contour and fuzzy-based level-set method for same set of images and concluded that proposed model method is more accurate and effective for clinical purpose.

Keywords: White corpuscles nucleus segmentation, region-based active contour, fuzzy-based level set method, U-Net model

1. Introduction

The diagnosis of blood-related diseases and corresponding treatment largely depends on the white blood cells (WBC) segmentation system. Medical segmentation of WBCs becomes tough when hematologists use visual identification under the light microscope due to asymmetrical morphological structure, shapes, and sizes of WBCs [1]. The manual segmentation of WBCs performed by hematology specialists is a tedious and too long process. Therefore, there is a need for automated WBCs seg-

mentation tools in the medical disease diagnosis system. In the last few years, progresses in computer oriented automatic frameworks have led to quicker and additional reproducible medical images examine than physical examination [2, 3]. Various automated segmentation models have been proposed and used for medical image examination. They are mostly based on some popular methods such as clustering algorithms, thresholding, region-based methods, edge-based methods, Watershed transform, and deep learning methods.

Since manual medical image segmentation is sophisticated as well as not accurate, a lot of computer-assisted automatic segmentation models have been proposed. In the beginning, rule-based methods were proposed and successfully applied.

---

*Corresponding author. Indrajeet Kumar, Graphic Era Hill University, CSE department, Dehradun, India. E-mail: erindrajeet@gmail.com.

Table 1
Various WBC segmentation methods and corresponding
techniques used in past

Method	Technique
Clustering algorithms	SFC- means [7]
	K-means [5, 6]
	Fuzzy C-means [9, 10]
Thresholding methods	Otsu thresholding [10]
	Zack's algorithm [11]
	Stepwise averaging technique [12]
	Color threshold [13]
	Histogram-thresholding [14]
	Adaptive thresholding [41]
Edge-based	Edge detector [16]
	Grabcut approach [40]
Region-based	Region growing [15]
	Region based active contour [7]
Deep learning-based models	DCNN [22]
	Segnet [20]
	Convolution Neural Networks [22–24]
	CNN [24]
Other algorithms	k-NN [17]
	Watershed transform [18]

Note: SFC: spatial fuzzy c-mean CNN: Convolutional Neural Network; C-KNN: Customized KNN, DCNN: Deep CNN.

Table 2
Description of past studies carried out for leukocyte segmentation
using deep learning models

Reference, year	DL Model	No. of Images	Accuracy (%)
[20], 2018	SegNet + VGC-16	45	91.11
[21], 2018	C-KNN	80	96.25
[22], 2019	Hybrid segmentation	260	98.70
[23], 2019	RCNN + FPN	300	99.54
		100	99.43
		268	98.94
		257	98.44
[24], 2020	CNN	260	98.61
[37], 2019	CNN	94	93.60
[38], 2020	U-Net	599	62.50
[39], 2019	R-CNN + U-Net	599	63.33
Proposed work	DCNN + U-Net	260	99.02

However, these methods could not justify the robustness of a wide variety of data [4]. Thus, the numbers of adaptive algorithms based on color, shape, and region were proposed. The adaptive methods such as clustering algorithms [5–9], thresholding-based methods [10–14], edge-based methods [17], region-based methods [7, 15], and watershed transform [18, 19] have been used for segmentation of blood images by the researchers.

It has been also analyzed that there are some significant drawbacks to the existing WBC segmentation system. The Post-processing stage does not deal well with varied kinds of input images. Since blood images can be affected by the light intensities and staining process, that can degrade the segmentation rate. Apart from this, the low accuracy and the higher processing time are also limitations of using these existing techniques. To overcome such type of issues, the convolution neural network (CNN) based model is proposed to segment WBCs efficiently.

Table 1 shows the different segmentation methods and techniques used in past studies.

From past studies, it has been found that the prior knowledge of the cluster size while using the non-adaptive k-means technique is known [5, 6]. The research reported in [6] concludes that the K-means technique with CMYK does not work well with noisy input images; therefore, pre-processing is an essential step. Otsu's thresholding technique is also popular in the field of segmentation, but dependency on Otsu's

threshold makes it a specific-purpose segmentation technique [10]. One shortcoming of using k-NN is required to compute the value of parameter k, and the cost of computing k is quite high [17]. Most of the above segmentation techniques could not be able to handle the variance in real word existing data and also suffer from human biases. Modern developments in deep learning models have shown several promises towards solving such problems.

The CNNs [22–24] and SegNet [19, 20], have been found useful in the field of object classification and semantic segmentation. Since deep learning methods are more intuitive in performing semantic segmentation, researchers have done a lot of research in leukocyte nucleus segmentation. The list of past studies carried out for leukocyte segmentation using deep learning models is given in Table 2.

Table 2 shows that the deep learning-based models perform significantly well in semantic segmentation with higher accuracy. Despite everything, one major limitation of the above model is that they need a massive amount of training data. If there is a smaller number of training samples, they need a low amount of variance in training data. Unfortunately, the acquisition of the medical image is expensive and complicated. However, deep learning methods have shown immense outcome in the domain of bio-medical image segmentation in last five years, and in most of the research, it is found that U-Net did far better than other CNNs [25]. The architecture of U-Net and SegNet is very similar, comprising the down-sampling phase and an up-sampling phase. Besides, the identical level layers of these two phases are linked by concatenation operations, before a pooling operation and after a de-convolution process respectively.

It is found that the U-Net model has enough potential to segment bio-medical images, even with a smaller number of training data. U-Net based model has shown success in segmenting the biomedical image of Skin-Lesion [26], histology [27], kidney [28], neuronal structure [29], liver and tumor [30], lung lobe [31] and so on. Therefore, the proposed method is based on the U-Net model and enhances the result of nucleus segmentation in all aspects.

1.1. Proposed work contributions

Based on the deep study of literature, the major contributions of the work is as follows:

- i. Deep neural network based technique is proposed for automated WBC nucleus segmentation from given microscopic blood smear images.
- ii. The literature studies show that the limited number of work had been done using deep learning model and experience either low accuracy or high complexity. So to enhance the diagnostic potential of blood related disorders, proposed work accounts a significant role.
- iii. To analyze the results yielded by proposed work, implementing deep learning-based CNN to segment the WBC nucleus form given microscopic blood smear images.
- iv. The results attained by used model is compared with previously published work and results obtained in our model outperform existing works for in terms of accuracy, sensitivity, specificity, Jaccard index, dice coefficient, and structure similarity index.

2. Dataset and methodology

2.1. Dataset description and preparation

In this work, the ALL-IDB blood dataset is considered, which contains 2592×1944, an original resolution ROI images with 24-bit color depth. The database has two different kinds of the database (ALL-IDB-1 and ALL-IDB-2) mainly for classification and segmentation task.

The ALL-IDB-1 dataset [32] is useful for validating the segmentation and classification performance of deep learning methods. The dataset contains 108 images labeled by expert oncologists with 39000 blood elements. Figure 1 presents two images from

Table 3
Description of the dataset

Parameter	Dataset	
	ALL-IDB-1	ALL-IDB-2
Number of Samples	109	260
Native Resolution	2592×1944	257×257
Total Number of Elements	39000	260
Number of Lymphoblast	510	130

the ALL-IDB-1. The blood in the first image belongs to healthy people and the blood of the second image belongs to people affected by acute lymphoblastic leukemia (ALL).

The ALL-IDB-2 dataset [33] is specially designed for testing the performance of the segmentation system. The dataset is a set of samples fit in to the ALL-IDB-1 dataset with the cropped region of interest of each case. The total no. of cropped images in the dataset is 260 images, and the half of the dataset corresponds to lymphoblast.

Figure 2 shows four healthy and four probable blast cells from the ALL-IDB2 dataset. The brief description of ALL-IDB-1 and ALL-IDB-2 is also given in Table 3.

2.2. Region-based contour method

The main objective of using a region-based active contour method is to determine area of interest by using some region initiator to initiate the action of the active contour [15]. The method deals with two forces; minimization of energy based on statistical nature and curvature movement created by the level-set function and commonly denoted by $\varphi(x, y)$. The extraction of intensity information within the local region helps monitor the contour's action toward the object. The differential equation is given in Equation 1.

$$\frac{\partial \varphi}{\partial t} = XX + YY$$

$$XX = -\delta\varepsilon(\varphi)(\beta 1 e 1 - \beta 2 e 2)$$

$$YY = w\delta\varepsilon(\varphi)div\left(\frac{\nabla\varphi}{|\nabla\varphi|}\right) + \mu\left(\nabla^2\varphi - div\left(\frac{\nabla\varphi}{|\nabla\varphi|}\right)\right)$$
$$(1)$$

In the above differential equation, the first term defines the propagation of the active contour within the object's boundary, and the next term works on smoothing the contour. The last term is level-set regularization, which maintains the regularity of this function close to the actual distance function. The
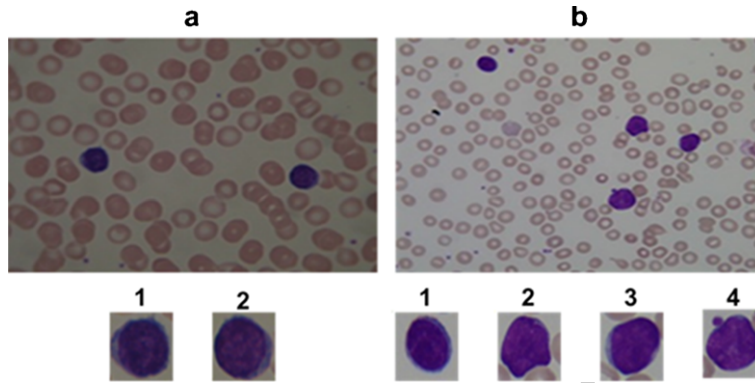
a   **b**

1   **2**   **1**   **2**   **3**   **4**

Fig. 1. (a) Healthy people's blood, (b) blood of people affected by ALL. (a1-4) and (b1-4) are cropped subplot of the (a) and (b).

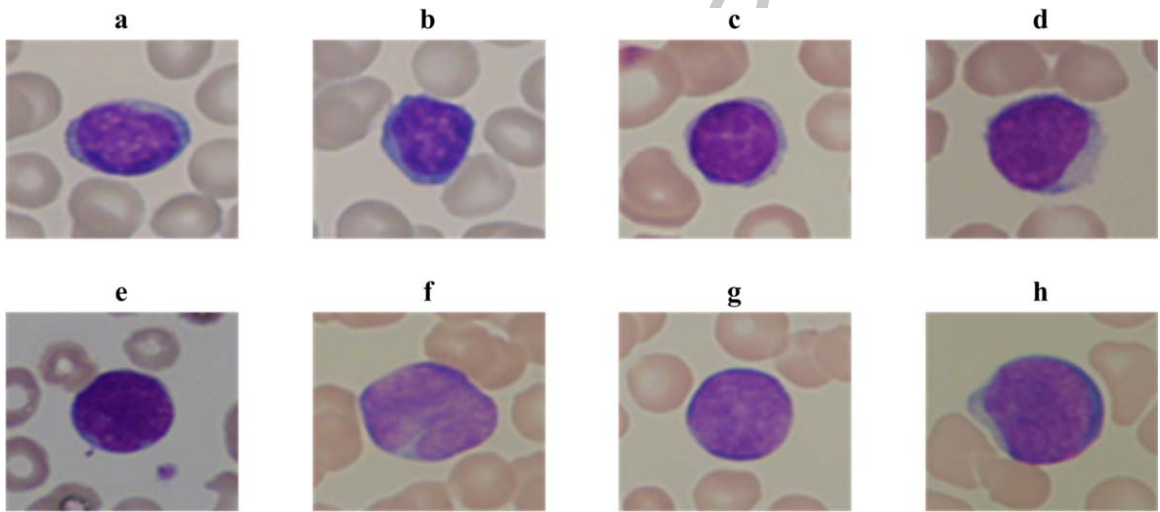**a**   **b**   **c**   **d**

e   **f**   **g**   **h**

Fig. 2. Images of ALL-IDB2 dataset- (a-d) healthy cells, (e-h) lymphoblast from ALL patients.

term $\beta 1$, $\beta 2$, w, and μ are known as the weighting coefficient to their corresponding term. $\delta\varepsilon(x)$ represents the Dirac function and also known as derivative of Heaviside function ($H\varepsilon(x)$). The mathematical representation of these two functions as:

$$H\varepsilon(x) = \frac{1}{2}\left[1 + \frac{2}{\pi}\tan^{-1}\left(\frac{x}{\varepsilon}\right)\right] \qquad (2)$$

$$\delta\varepsilon(z) = \frac{1}{\pi}\frac{\varepsilon}{\varepsilon^2 + x^2} \qquad (3)$$

Here ε denotes a constant term which regularizes the Dirac function.

Let E_i denote the inner contour energy function, and E_O denotes the outer contour energy function. Then, energy functions defined as:

$$Ei(x) = \int K\alpha(y - x)|I(x) - f1(y)|^2 dy \qquad (4)$$

$$E_O(x) = \int K\alpha(y - x)|I(x) - f2(y)|^2 dy \qquad (5)$$

Where $f1$ and $f2$ represent functions of contour fitting of y and mathematically defined as:

$$f_1(y) = \frac{K\alpha\left[H\varepsilon(\varphi(y))I(y)\right]}{K\alpha[H\varepsilon(\varphi(y))]} \qquad (6)$$

$$f_2(y) = \frac{K\alpha[(1 - H\varepsilon(\varphi(y)))I(y)]}{K\alpha[(1 - H\varepsilon(\varphi(y)))]} \qquad (7)$$

Where $K\alpha$ denotes Gaussian kernel and is formulated as:

$$K\alpha(z) = \frac{1}{(2\pi)^{n/2}\alpha^n}e^{-|z|^2/2\alpha^2} \qquad (8)$$

Where α is the scalar parameter and always greater than zero.

The initialization of level-set function $\varphi_0(x, y)$ in region-based contour method, is mathematically defined as:

$$\varphi_0(x, y) = \begin{cases} c, & (x, y) \in Ci \\ -c, & (x, y) \notin Ci \end{cases} \quad (9)$$

Where c refers to a constant value and must be higher than 2ε, C_i represents the first contour with a positive value of $\varphi_0(x, y)$. The Equation (1) can be written in the following iterative form as:

$$\varphi_{x,y}^{t+1} = \varphi_{x,y}^t + \tau \frac{d\varphi_{x,y}^t}{dt} \quad (10)$$

Where τ is, the time step and the value of the time step can be taken large. For stability in level set evaluation, the cost of time step τ must satisfy the condition $\mu \times \tau < 1/4$, where μ is penalty term.

2.3. Fuzzy-based level set segmentation

In this method, the combination of the region-based contour and the fuzzy clustering method are used. The output of fuzzy clustering is useful for initializing the level-set procedure and finding the suitable value of the controlling parameters that control the progression of the level-set function [7]. If $Ui, j = [ui, j]$ denotes the membership function and $Z_{i,j}$ represents the binary image, which fetches object of interest from the input image.

$$z_{i,j} = \begin{cases} 1, & ui, j \geq b0 \\ 0, & otherwise \end{cases} \quad (11)$$

b_0 represents the adjustable threshold between 0 to 1.

Now, initialization of level-set function may be defined as:

$$\varphi_0(x, y) = 2\varepsilon(2Zi, j - 1) \quad (12)$$

Where, ε denotes a constant, which works on the Dirac function.

From prior level-set techniques, it can be observed that some controlling parameters are manually applied, and their values may vary according to the case. In this method, the estimation of controlling parameters is adaptively done by using outputs of fuzzy clustering. The Dirac function and the Heaviside function are useful to calculate the length and the area of the contour generated by the fuzzy clustering.

$$C_{length}(\varphi = 0) = \int_\Omega \delta 0(\varphi(x, y)) \,|\nabla \varphi(x, y)|dxdy \quad (13)$$

Where $\delta(\varphi)$ represents the Dirac function and defined as:

$$\delta 0(\varphi) = \frac{d}{d\varphi}H(\varphi) \quad (14)$$

Where $H(\varphi)$ represents the Heaviside function and using this, the area of the contour can be computed as:

$$C_{Area}(\varphi \geq 0) = \int_\Omega H(\varphi(x, y)dxdy \quad (15)$$

$$H(\varphi) = \begin{cases} 1, & if\varphi \geq 0 \\ 0, & if\varphi < 0 \end{cases} \quad (16)$$

It is analyzed that multiplication of the time step of level-set evolution (τ) and the regularization coefficient (μ) must be less than 0.25 for stability. The time step can be defined as:

$$\tau = \frac{C_{Area}}{C_{Length}} \quad (17)$$

The relationship between regularization coefficient and the time step can be defined as:

$$\mu < \frac{1}{4\tau} \quad (18)$$

The first part of the Equation (1) enhances the speed of working of level-set process toward the object. The value of β_1 and β_2 computed from the outputs of the fuzzy clustering is $0.5\text{-}u_{i,j}$ and the value of v is computed equals to 0.2τ.

2.4. Proposed work

2.4.1. Proposed workflow diagram

The flow chart of the work for nucleus segmentation is shown in Fig. 3. It comprises of Pre-processing phase, the U-Net model phase, and the post-processing phase. In this model, the pre-processing step is used to resize all the input images into $128 \times 128 \times 3$ pixels and corresponding masks into $128 \times 128 \times 1$ pixels and then normalization is done on all the images. After the pre-processing, the training dataset applied on the U-Net model and a segmented mask corresponding to their input
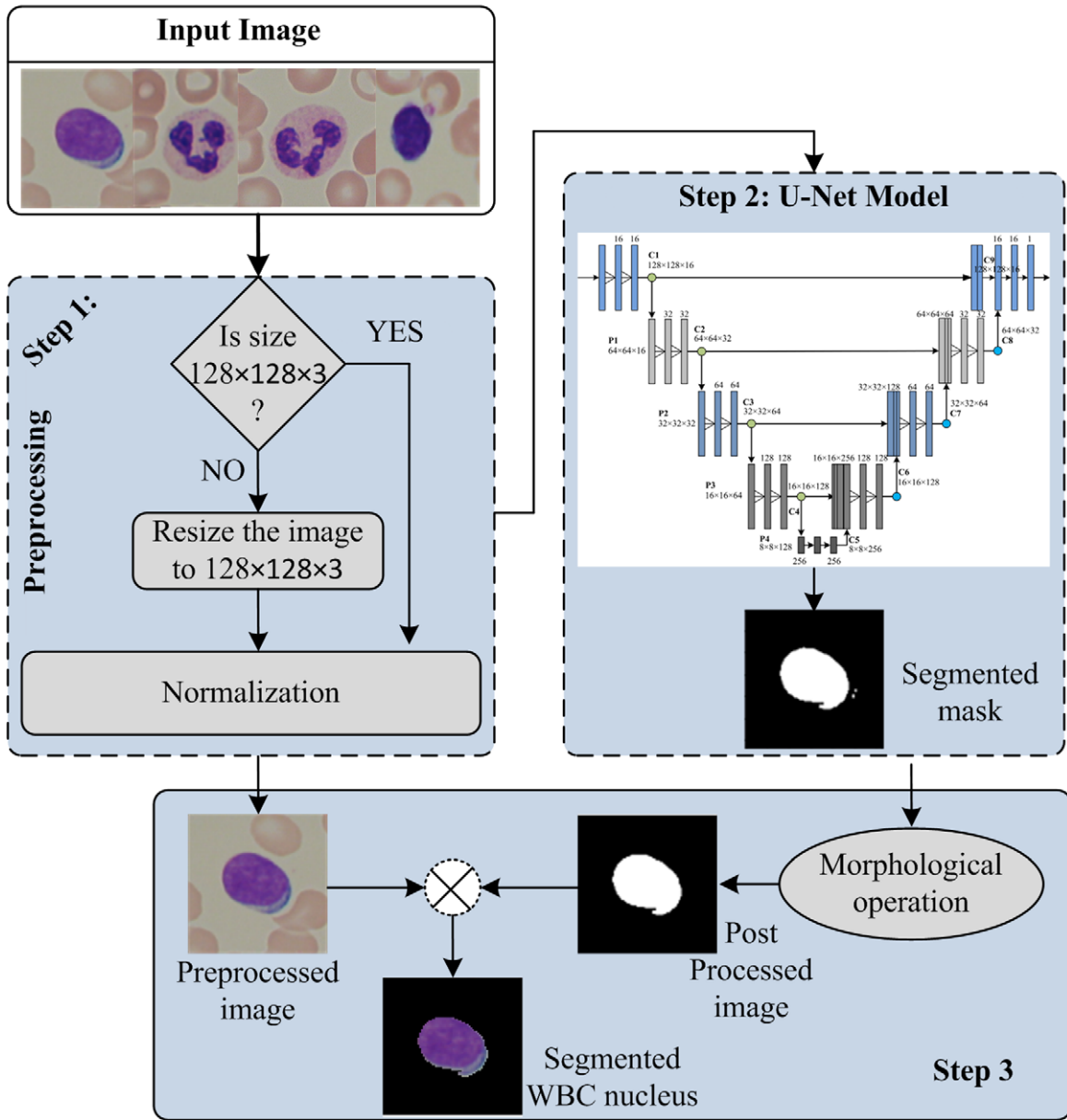
Fig. 3. Proposed workflow diagram.

image is generated by the trained model. Later, post-processing operation is performed on a generated mask for removing negative pixels, and element-wise multiplication is done to get the final segmented nucleus. The brief description of each phase is presented in the upcoming subsections.

2.4.2. Preprocessing

The pre-processing phase includes image normalization and resizing operation on all the input images.

Image normalization is a technique in image processing deals with the range of pixel intensity values, and it also ensures that each input parameter has an equal distribution of data. To prevent early saturation of sigmoid function, normalization is done by dividing RGB input images by 255 to scale the intensities within [0, 1].

The ALL-IDB dataset contains images of different sizes; therefore, the resizing operation is required to get a base size to all RGB input images and the

mask images. This step converts the dimension of all RGB input images into $128 \times 128 \times 3$ pixels and the images of the masks into $128 \times 128 \times 1$ pixels.

2.4.3. The proposed U-Net model

As the past studies show, the performance of the CNN based U-Net model is outstanding in semantic segmentation. Therefore, the proposed work is based on the U-Net model and has subtle differences from the original model. The architecture is symmetric, having the down-sampling phase and the up-sampling phase. The down-sampling level pulls out spatial attributes, from the input image and the up-sampling level creates the segmentation map using the encoded attributes. The down-sampling level consists of a series of two $[3 \times 3]$ convolution operations and a max-pooling operation stride of 2. The similar step is repeatedly applied in four levels, and the number of filters in the each level is doubled after each down-sampling.

Suppose $g_{n \times n}^2(\cdot)$ represents the convolution layer with strides of 2 and $p_{3 \times 3}^2(\cdot)$ denotes the max-pooling layer with strides of 2. The mathematical formula for output of the $l + 1th$ layer in down-sampling phase is:

$$x_{l+1} = g_{1 \times 1}(G_1) \circ g_{3 \times 3}^2(G_2) \circ p_{3 \times 3}^2(x_l)))$$
$$G_1 = g_{3 \times 3}^2(g_{1 \times 1}(x_l) \qquad (19)$$
$$G_2 = g_{3 \times 3}(g_{1 \times 1}(x_l))$$

At the bottom, a series of two $[3 \times 3]$ convolution operations work as the connector between the up-sampling and the down-sampling phases. On the other side, the up-sampling level firstly up the attribute map using transposed convolution operation and half the channel attributes. This phase also involves a series of two $[3 \times 3]$ convolution operations. The similar step is repeatedly applied in four times with half number of filters in each up-sampling.

For up-sampling, let convolution transposed layer is denoted by $t_{n \times n}^2(\cdot)$ with strides of 2 and the up-sampling layer is denoted by $u^2(\cdot)$ with strides of 2. Then, the mathematical formulation for output of the $l + 1th$ layer in up-sampling phase is:

$$x_{l+1} = t_{1 \times 1}(T_1) \circ t_{3 \times 3}^2(T_2) \circ u^2(x_l)))$$
$$T_1 = t_{3 \times 3}^2(t_{1 \times 1}(x_l) \qquad (20)$$
$$T_2 = t_{3 \times 3}(t_{1 \times 1}(x_l))$$

Finally, the output segmentation map is generated by performing a $[1 \times 1]$ convolution operation. One more useful prime attribute of the U-Net model is the U-shape skip connections. Prior to the pooling operation, the convolution layer's output in each level of the down-sampling phase is transmitted to the corresponding up-sampling level. Transmitted attributes are concatenated with the up-sampling level output, and the concatenated attribute map is transmitted to the succeeding layers. After each pooling operation, there is the loss of some spatial data, and the skip connections permit the model to fetch those lost data [33].

The proposed U-Net model uses the ReLU non-linear activation function in all convolution layers except the last one [34]. The non-linear activation method used in the final convolution layer is sigmoid as the work is dealing with only two classes. Since the model working with binary labels, so the loss function used is binary cross-entropy. An Adam optimizer is used in the model for maintaining the learning rate in each network weight. The pictorial representation of proposed U-Net model is shown in Fig. 4.

2.4.4. Post-processing

The result generated by the proposed U-Net model contains some invalid pixels. The invalid pixels are removing with the help of morphological transformation. This transformation includes some simple operations that depend on the structure and shape of the image and generally performed on binary images [35]. It needs two inputs: the primary image and the second one is a structuring component (SC), which decides the nature of the operation. The morphological opening is applied by using a structuring component. The objects in the input binary image $Z(x, y)$ are processed depending on attributes of the shape of the image, encoded in the structuring component. Erosion function can be obtained by $E(x, y)$.

$$E(x, y) = Z(x, y) \ominus SC(x, y)$$
$$= [a : SC(x, y)_a \subseteq \{Z(x, y)] \qquad (21)$$

Here $Z(x, y)$ denotes the binary image and $SC(x, y)$ denotes a structuring component. On the basis of size and shape of $SC(x, y)$, expanding of object in the image is done by using dilation $D(x, y)$.

$$D(x, y) = Z(x, y) \oplus SC(x, y)$$
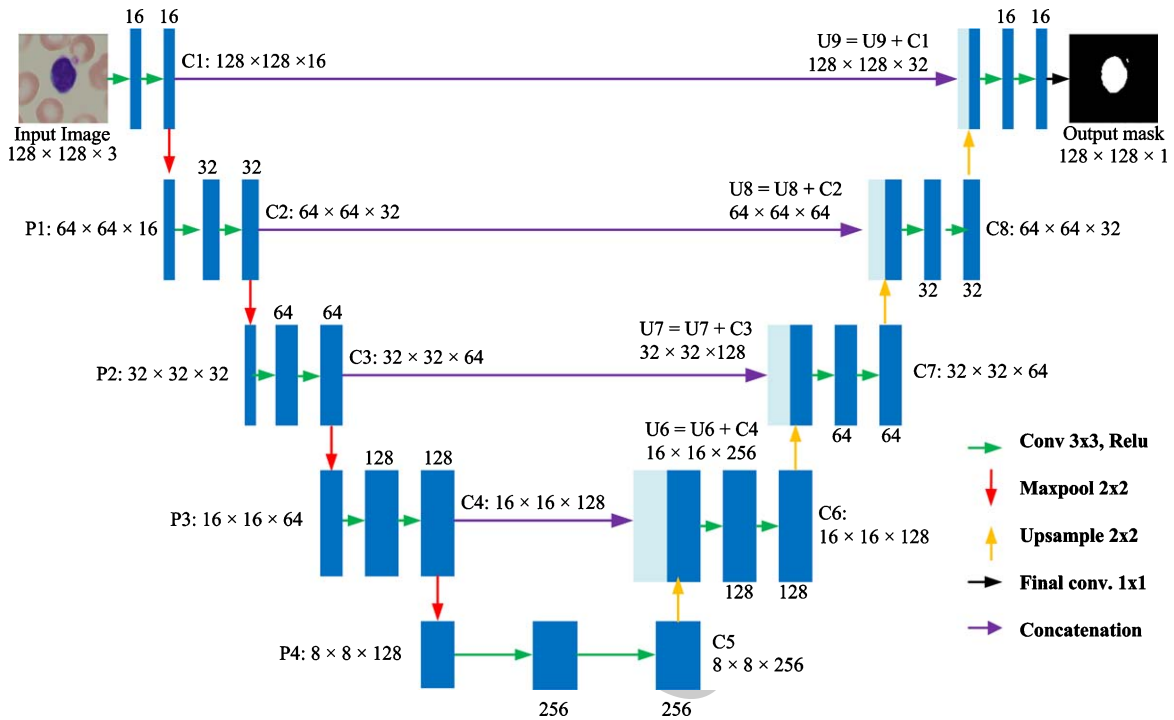$$= \{a : [(SC(x, y)a \cap Z(x, y)] \subseteq Z(x, y) \qquad (22)$$

Fig. 4. The architecture of proposed U-Net model.

The erosion function followed by dilation known as morphological opening (MO).

$$MO = E(x, y) \circ D(x, y)$$
$$= [Z(x, y) \ominus E(x, y)] \oplus D(x, y) \quad (23)$$

After preprocessing, the element wise multiplication is done between the post-processed segmented mask and resized input image

2.4.5. Staging analysis metrics

The staging analysis of each experiment is done according to quantitative parameters such as sensitivity, specificity, Jaccard Index, Dice-coefficients, accuracy, and structural similarity index (SSIM) [37]. The mathematical expression for each parameters is given in Equations 24 to 29, respectively.

$$Sensitivity(\%) = \left[\frac{TP}{TP + FN} \right] \times 100 \quad (24)$$

$$Specificity(\%) = \left[\frac{TN}{TN + FP} \right] \times 100 \quad (25)$$

$$Accuracy(\%) = \left[\frac{TP + TN}{TP + FP + FN + TN} \right] \times 100 \quad (26)$$

$$JaccardIndex(\%) = \left[\frac{IGT \cap IUS}{IGT \cup IUS} \right] \times 100 \quad (27)$$

$$DiceCoefficient(\%) = \left[2 \times \frac{IGT \cap IUS}{IGT + IUS} \right] \times 100 \quad (28)$$

Note: TP: pixels present in both the ground truth segmented region and segmented region generated by the model, FN: area present in the ground truth segmented region but not present in the segmented area created by the model, TN: area absent in both ground truth segmented region and segmented area detected by the model, and FP: area missing in ground truth segmented region, but the area present in the segmented area recognized by the model. I_{GT} denote the ground truth segmented area of the image and I_{US} means the segmented field by the proposed model

SSIM: Structural Similarity Index is useful to find out the loss in image quality caused by processing. It calculates the difference between ground truths segmented image and the segmented image by the model. This value is computed on different windows of a copy. Let window x and y of standard size n × n, M_x denotes mean of x, $\sigma^2 x$ represents the variance of x and σ_{xy} denotes the covariance of x and y. The mathematical formula derived for SSIM if all weights are equal to 1 is given by

$$SSIM = \frac{\left(2M_x M_y + V_1\right)\left(2\sigma xy + V_2\right)}{\left(M_x^2 + M_y^2 + V_1\right)\left(\sigma_x^2 + \sigma_y^2 + V_2\right)} \tag{29}$$

Where, V_1 and V_2 are two variables which provide stability to division even with weak denominator. There are three major component measurement between x and y samples in SSIM; luminance $(l_{x,y})$, contrast $(c_{x,y})$ and structure $(s_{x,y})$. The formula for individual functions as:

$$l_{x,y} = \frac{2M_x M_y + c1}{M_x^2 + M_y^2 + c1} \tag{30}$$

$$c_{x,y} = \frac{2\sigma_x \sigma_y + c2}{\sigma_x^2 + \sigma_y^2 + c2} \tag{31}$$

$$s_{x,y} = \frac{\sigma_{xy} + c3}{\sigma_x \sigma_y + c3} \tag{32}$$

3. Experiments and results

3.1. Environmental setup

The complete set of experimentation is carried out at HP Z4 G4 workstation. The system specification is given as Intel Xeon W-2014 CPU @ 3.2 GHz processor, having RAM of 64 GB, 4GB of NVIDIA Quadro P1000 graphics, 256 GB SS, and 2TB SATA HDD. All images are stored at this system, and the Python environment is used for performing the experiments.

3.2. Experiment description

In this work, three extensive experiments have been performed using blood smear taken from the ALL-IDB2 dataset. The brief description of the experiments carried out for this work is explained in subsequences.

3.2.1. Experiment 1

In this experiment, a region-based active contour method is used. The theoretical description of the active contour model is discussed in section 3.2 of the manuscript. For white corpuscles nucleus segmentation from blood smear images, the ALL-IDB-2 dataset is used. The sample of the segmented nucleus is shown in Fig. 6, and the quantitative analysis of randomly selected twenty blood smear is given in Tables 5 and 6.

Table 4
Training and Testing performance of Model1 to Model5

Model no. #	Bifurcation ratio	Training		Testing	
		Acc. (%)	Loss	Acc. (%)	Loss
Model1	50:50	98.03	0.0651	98.22	0.0584
Model2	60:40	98.45	0.0520	98.62	0.0450
Model3	70:30	98.51	0.0496	98.28	0.0558
Model4	80:20	98.61	0.0443	98.47	0.0567
Model5	90:10	98.69	0.0429	99.02	0.0310

3.2.2. Experiment 2

For this experiment, the fuzzy-based level set method is considered. The critical conceptual description of the fuzzy-based level set method is already discussed in section 3.2 of this manuscript. For white corpuscles nucleus segmentation from blood smear images, the ALL-IDB-2 dataset is used. The sample of the segmented nucleus is shown in Fig. 6, and the quantitative analysis of randomly selected twenty blood smears segmented by a fuzzy-based level set method is given in Tables 5 and 6.

3.2.3. Experiment 3

In this experiment, extensive work has been carried out for white corpuscles nucleus segmentation from blood smear images using a deep CNN (proposed) method. The structure and working of the proposed model are previously discussed in Section of the manuscript. Initially, input images taken from ALL-IDB-2 dataset and their mask labeled by medical expert used as a ground truth mask is passed to the model. The complete set of images is bifurcated into two sets called training and testing set in five different ratios i.e., 50/50, 60/40, 70/30; 80/20 and 90/10. The trained and validated model using a set 1 having ratio of 50/50 is named Model1. In the same manner, Model2, Model3, Model4, and Model5 are trained and validated using ratio 60/40, 70/30; 80/20 and 90/10, respectively. The training and testing performance of each model is computed in terms of accuracy and loss. The obtained value of each model for the training and testing phase is reported in Table 4.

From Table 4, it has been found that Model 5 performs outstandingly with respect to other models. The training accuracy and loss for model5 are 98.69 %, and 0.0429 and testing accuracy and loss is 99.02 % and 0.0310, respectively. The training and testing data bifurcation ratio is 90/10. It is also noticed that the training accuracy is increasing in order while the number of testing samples is increased. The training
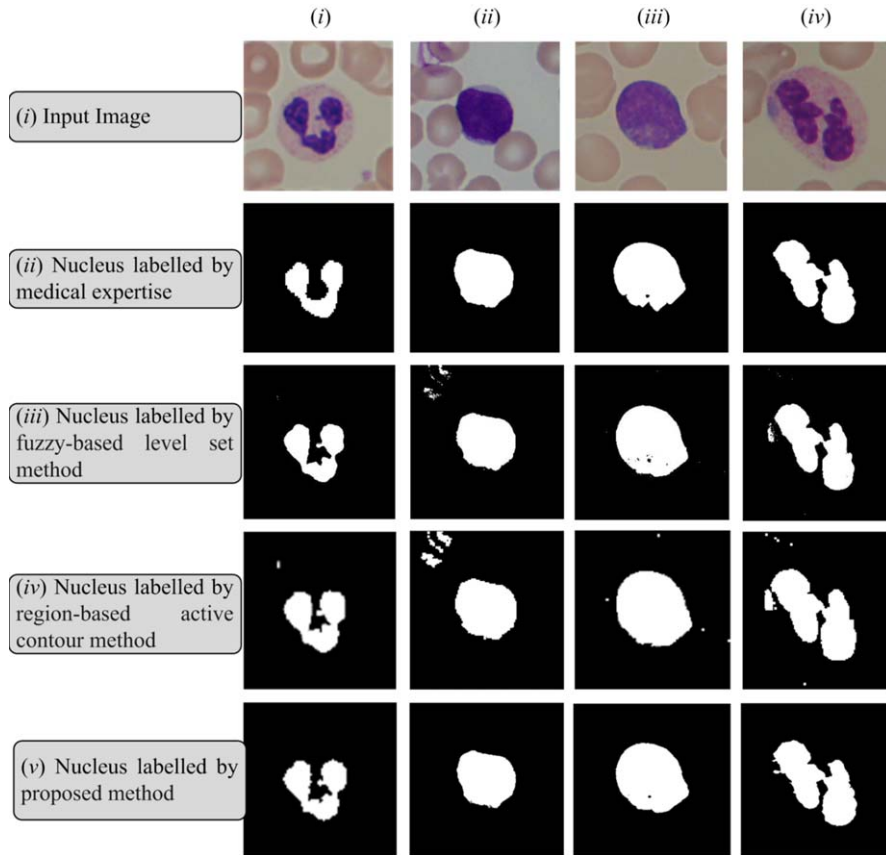
Fig. 5. Segmented nucleus.

and testing performance curve for each model is shown in Fig. 5.

In this experiment, five different segmentation models have been created, and the best performing model is selected. The training phase learning curve and testing phase learning curve for each model is shown in Fig. 6. From Table 4, it has been observed that Model5 is the best performing model in terms of training and testing accuracy. The randomly selected twenty images are passed to selected model 5, and obtained results are given in Tables 5, and 6.

The obtained quantitative performance of experiment 1 to experiment 3 for randomly selected twenty test samples are reported in Table 5 in terms of sensitivity, specificity and, Jaccard index, Table 6 in terms of Dice-coefficients, accuracy and SSIM.

3.3. Result analysis

The quantitative analysis of the experiments carried out for the work is done in the form of sensitivity, specificity, Jaccard index, Dice-coefficient, accuracy, and SSIM. The obtained result from experiments is reported in Tables 5, and 6.

Table 5 reports the results of experiment 1, experiment 2, and experiment 3 in terms of sensitivity, specificity and Jaccard index. It shows the obtained average sensitivity for randomly selected twenty images is 88.81 %, 89.79 %, and 90.32 % for experiment 1, experiment 2, and experiment 3 respectively. For the same set of testing samples, obtained average specificity value for experiment 1, experiment 2, and experiment 3 is 68.82 %, 85.99 %, and 95.09 %, respectively.

The obtained value of the Jaccard index and Dice-coefficient for experiment 1, experiment 2, and experiment 3 is reported in Tables 5 and 6. The obtained value of the Jaccard index is 68.89 %, 91.27 %, and 91.50 % using region-based active contour method, fuzzy-based level set method, and proposed model. For the same set of randomly selected twenty test instances, the obtained Dice-coefficient is 81.07
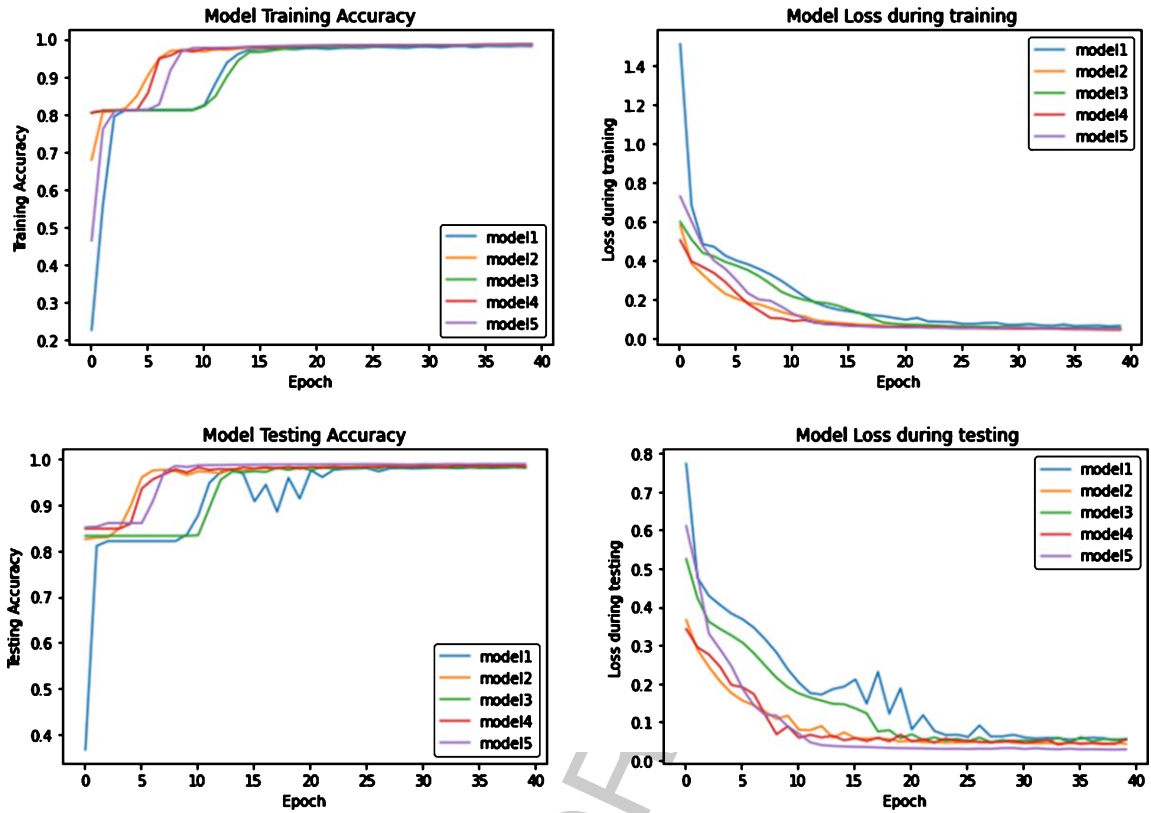
Fig. 6. Resultant curve for the accuracy and loss with no. of epoch.

Table 5
Quantitative performance of experiment 1, experiment 2 and experiment 3 in terms of sensitivity and specificity

Image no.	Sensitivity (%)			Specificity (%)			Jaccard Index (%)		
	Experiment 1	Experiment 2	Experiment 3	Experiment 1	Experiment 2	Experiment 3	Experiment 1	Experiment 2	Experiment 3
1	93.61	94.49	83.75	93.11	96.54	100	87.59	94.67	83.75
2	89.91	91.38	86.35	47.78	90.18	99.73	59.07	92.15	86.12
3	89.81	90.67	91.46	96.75	93.52	98.78	86.99	91.24	91.35
4	97.75	98.10	91.33	96.54	92.69	97.59	94.49	98.23	91.56
5	95.04	96.22	87.88	93.65	90.92	98.65	89.37	96.54	97.68
6	97.12	97.40	89.38	77.42	92.19	97.24	79.23	97.59	89.38
7	89.54	89.69	90.07	57.93	85.21	95.46	63.03	91.02	90.07
8	93.32	93.64	86.59	46.79	89.87	89.51	60.91	94.23	86.23
9	95.25	95.65	86.32	51.39	87.14	88.82	64.09	96.14	84.78
10	90.79	90.84	88.35	56.35	86.23	99.93	63.20	91.95	96.54
11	90.28	91.95	89.92	59.06	85.21	96.24	64.06	92.98	88.72
12	83.97	85.47	90.28	72.11	79.13	96.21	65.66	87.98	93.56
13	90.26	90.39	91.20	45.27	90.76	95.87	58.33	91.20	94.23
14	63.43	65.77	91.34	81.93	72.93	91.05	53.72	73.07	96.14
15	83.07	86.16	92.69	61.99	83.19	91.35	60.19	88.15	92.54
16	80.47	82.38	91.09	83.42	72.81	90.42	69.02	86.14	93.52
17	92.02	93.09	93.26	63.20	82.56	92.84	67.27	94.11	92.86
18	84.69	85.46	94.23	70.75	80.85	93.87	65.53	87.80	91.74
19	86.97	87.51	96.56	62.83	82.39	94.68	63.40	89.38	95.42
20	88.96	89.58	94.36	58.21	85.53	93.59	62.74	90.89	93.84
Avg.	**88.81**	**89.79**	**90.32**	**68.82**	**85.99**	**95.09**	**68.89**	**91.27**	**91.50**

Table 6
Quantitative performance of experiment 1, experiment 2 and experiment 3 in terms of sensitivity and specificity

| Image no. no.	Dice-Coefficient (%)			Accuracy (%)			Structural similarity Index (%)		
	Experiment 1	Experiment 2	Experiment 3	Experiment 1	Experiment 2	Experiment 3	Experiment 1	Experiment 2	Experiment 3
1	93.38	89.88	91.16	93.36	93.90	91.87	98.44	88.49	99.26
2	74.27	85.44	92.54	68.85	89.79	93.04	94.81	92.15	99.81
3	93.04	83.88	94.93	93.28	89.83	95.12	98.39	88.48	99.93
4	97.16	96.52	95.46	97.15	96.39	95.66	99.36	87.52	99.91
5	94.39	93.31	93.55	94.35	94.25	93.94	98.76	88.20	99.92
6	88.41	95.28	94.39	87.27	95.61	94.69	97.38	89.63	99.95
7	77.32	83.51	94.78	73.74	87.36	95.03	95.51	91.65	99.89
8	75.71	89.09	91.47	70.06	91.71	92.07	95.06	92.04	99.85
9	78.12	92.57	90.6	73.32	92.88	91.41	95.61	91.62	99.83
10	77.45	85.10	91.48	73.57	88.53	92.14	95.54	91.75	99.77
11	78.09	86.89	94.45	74.67	89.26	92.66	95.73	91.50	99.81
12	79.27	78.54	94.83	78.04	82.78	93.45	96.16	91.12	98.97
13	73.68	83.83	94.29	67.77	89.04	92.72	94.72	92.33	99.03
14	69.89	57.56	92.40	72.68	67.33	93.74	95.23	91.98	99.54
15	75.15	78.81	91.98	72.53	84.08	92.61	95.26	91.61	98.87
16	81.67	75.66	91.36	81.94	79.25	92.30	96.80	90.58	97.86
17	80.43	88.88	92.95	77.61	89.66	93.06	96.41	91.38	99.54
18	79.17	78.25	93.43	77.72	83.09	92.99	96.06	91.21	99.61
19	77.60	80.80	95.34	74.90	85.02	95.99	95.72	91.47	99.32
20	77.11	83.31	93.85	73.59	87.33	94.10	95.56	91.74	99.97
Avg.	**81.07**	**84.36**	**93.26**	**78.82**	**87.85**	**93.43**	**96.33**	**90.82**	**99.53**
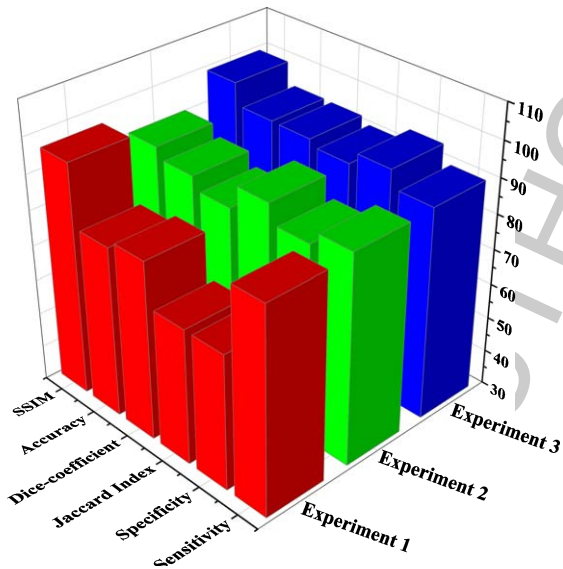
Fig. 7. Comparative analysis of each experiment.

%, 84.36 % and 93.26 % using region-based active contour method, fuzzy-based level set method, and proposed model.

After successful execution of tedious experiments for white corpuscles nucleus segmentation using region-based active contour method, fuzzy-based level set method, and the proposed method, the obtained value of accuracy and SSIM for twenty test samples is reported in Table 6. From Table 6, the accuracy value for experiment 1, experiment 2, and experiment 3 is 78.82 %, 87.85 %, and 93.43 % respectively. In the same manner, 96.33 %, 90.82 %, and 99.53 % of SSIM are achieved for region-based active contour method, fuzzy-based level set method, and proposed method. The comparative analysis of each experiment is shown in Fig. 7.

Quantitative analysis of the experiments carried out for the work is reported in Tables 5, and 6. It has been observed that the proposed model yields the highest sensitivity are 90.32 %, sensitivity is 95.09 %, Jaccard index is 91.50 %, dice-coefficient is 93.26 %, accuracy is 93.43 %, and SSIM index is 99.53 %. It shows that the performance of the proposed model is useful compared to popular segmentation techniques region-based active contour method and fuzzy-based level set method.

4. Conclusion

The proper identification of the WBC nucleus is one of the vital tasks because of the asymmetrical morphological structure, shapes, and sizes of WBC nucleus. The earlier developed WBC nucleus segmentation system's efficiency and accuracy depend on hematologist experience and image quality of collected blood smear. To reduce the involvement

of hematologists, fully automated white corpuscles nucleus segmentation proposed using deep neural networks for microscopic blood smear images. Initially, five different deep neural network-based models are trained using different sets of training and testing datasets. Among the five models, the best performing model having accuracy of 99.02 % is selected and evaluated randomly picked twenty test instances based on sensitivity, specificity, Jaccard index, Dice-coefficient, accuracy, and SSIM. The experimental outcome proved that the segmentation model used in this work yields better performance compared with existing methods, including the region-based active contour and Fuzzy-based level set models. All the experiments highlighted that the proposed model architecture is a more suitable for WBC nucleus segmentation and also accounts significant role for blood order detection in clinical practice.

Acknowledgments

References

[1] B.J. Bain, A beginner's guide to blood cells, *Wiley* (2008). https://onlinelibrary.wiley.com/doi/abs/10.1002/97811193 67871.

[2] F. Xing and L. Yang, Robust nucleus/cell detection and segmentation in digital pathology and microscopy images: a comprehensive review, *IEEE Reviews in Biomedical Engineering* **9** (2016), 234–263. https://doi.org/10.1109/RBME.2016.2515127.

[3] J. Wen, Y. Xu, Z. Li, Z. Ma and Y. Xu, Inter-class sparsity based discriminative least square regression, *Neural Networks* **102** (2018), 36–47. https://doi.org/10.1016/j.neunet.2018.02.002.

[4] D.L. Pham, C. Xu and J.L. Prince, Current methods in medical image segmentation, *Annual Review of Biomedical Engineering* **2** (2000), 315–337. https://doi.org/10.1146/annurev.bioeng.2.1.315.

[5] J. Laosai and K. Chamnongthai, Acute leukemia classification by using SVM and K-Means clustering, In *2014 International Electrical Engineering Congress (iEECON)* (2014), (pp. 1–4). IEEE. https://doi.org/10.1109/iEECON.2014.6925840.

[6] F. Kazemi, T.A. Najafabadi and B.N. Araabi, Automatic recognition of acute myelogenous leukemia in blood microscopic images using k-means clustering and support vector machine, *Journal of Medical Signals and Sensors* **6** (2016), 183. http://www.jmssjournal.net/text.asp?2016/6/3/183/186885.

[7] H.S. Bhadauria and M.L. Dewal, Intracranial hemorrhage detection using spatial fuzzy c-mean and region-based active contour on brain CT imaging, *Signal, Image and Video Processing* **8** (2014), 357–364. https://doi.org/10.1109/iEECON.2014.6925840.

[8] S. Alferez, A. Merino, L. Bigorra, L. Mujica, M. Ruiz and J. Rodellar, Automatic recognition of atypical lymphoid cells from peripheral blood by digital image analysis, *American Journal of Clinical Pathology* **143** (2015), 168–176. https://doi.org/10.1309/AJCP78IFSTOGZZJN.

[9] M. MoradiAmin, A. Memari, N. Samadzadehaghdam, S. Kermani and A. Talebi, Computer aided detection and classification of acute lymphoblastic leukemia cell subtypes based on microscopic image analysis, *Microscopy Research and Technique* **79** (2016), 908–916. https://doi.org/10.1002/jemt.22718.

[10] S. Nazlibilek, D. Karacor, T. Ercan, M.H. Sazli, O. Kalender and Y. Ege, Automatic segmentation, counting, size determination and classification of white blood cells, *Measurement* **55** (2014), 58–65. https://doi.org/10.1016/j.measurement.2014.04.008.

[11] A.M. Abdeldaim, A.T. Sahlol, M. Elhoseny and A.E. Hassanien, Computer-aided acute lymphoblastic leukemia diagnosis system based on image analysis (2018). In *Advances in Soft Computing and Machine Learning in Image Processing (pp. 131–147). Springer, Cham.* https://doi.org/10.1007/978-3-319-63754-9_7.

[12] H. Cao, H. Liu and E. Song, A novel algorithm for segmentation of leukocytes in peripheral blood, *Biomed. Signal Process Control* **45** (2018), 10–21. https://doi.org/10.1016/j.bspc.2018.05.010.

[13] L.B. Toh, M.Y. Mashor, P. Ehkan, H. Rosline, A.K. Junoh and N.H. Harun, Image segmentation for acute leukemia cells using color thresholding and median filter, *Journal of Telecommunication, Electronic and Computer Engineering (JTEC)* **10** (2018), 69–74. http://repo.uum.edu.my/id/eprint/26883.

[14] X. Zhou, C. Wang, Z. Li and F. Zhang, Adaptive histogram thresholding-based leukocyte image segmentation (2020), In *Advances in Intelligent Information Hiding and Multimedia Signal Processing (pp. 451–459). Springer*, Singapore. https://doi.org/10.1007/978-981-13-9710-3_47.

[15] H. Yu, F. He and Y. Pan, A novel region-based active contour model via local patch similarity measure for image segmentation, *Multimedia Tools and Applications* **77** (2018), 24097–24119. https://doi.org/10.1007/s11042-018-5697-y.

[16] S. Arslan, E. Ozyurek and C. Gunduz-Demir, A color and shape based algorithm for segmentation of white blood cells in peripheral blood and bone marrow images, *Cytometry Part A* **85** (2014), 480–490. https://doi.org/10.1002/cyto.a.22457.

[17] B.K. Das and H.S. Dutta, Infection level identification for leukemia detection using optimized Support Vector Neural Network, *The Imaging Science Journal* **67** (2019), 417–433. https://doi.org/10.1080/13682199.2019.1701172.

[18] L.B. Dorini, R. Minetto and N.J. Leite, Semiautomatic white blood cell segmentation based on multiscale analysis, *IEEE*

Journal of Biomedical and Health Informatics **17** (2012), 250–256. https://doi.org/10.1109/TITB.2012.2207398.

[19] V. Badrinarayanan, A. Kendall and R. Cipolla, Segnet: A deep convolutional encoder-decoder architecture for image segmentation, *IEEE Transactions on Pattern Analysis and Machine Intelligence* **39** (2017), 2481–2495. https://doi.org/10.1109/TPAMI.2016.2644615.

[20] T. Tran, O.H. Kwon, K.R. Kwon, S.H. Lee and K.W. Kang, Blood cell images segmentation using deep learning semantic segmentation, In *2018 IEEE International Conference on Electronics and Communication Engineering (ICECE) (pp. 13–16). IEEE*. https://doi.org/10.1109/ICECOME.2018.8644754.

[21] D. Umamaheswari and S. Geetha, A Framework for Efficient Recognition and Classification of Acute Lymphoblastic Leukemia with a Novel Customized-Knn Classifier, *Journal of Computing and Information Technology* **26** (2018), 131–140. https://doi.org/10.20532/cit.2018.1004123.

[22] K.K. Jha and H.S. Dutta, Mutual Information based hybrid model and deep learning for Acute Lymphocytic Leukemia detection in single cell blood smear images, *Computer Methods and Programs in Biomedicine* **179** (2019), 104987. https://doi.org/10.1016/j.cmpb.2019.104987.

[23] H. Fan, F. Zhang, L. Xi, Z. Li, G. Liu and Y. Xu, LeukocyteMask: An automated localization and segmentation method for leukocyte in blood smear images using deep neural networks, *Journal of Biophotonics* **12** (2019), e201800488. https://doi.org/10.1002/jbio.201800488.

[24] P.P. Banik, R. Saha and K.D. Kim, An Automatic Nucleus Segmentation and CNN Model based Classification Method of White Blood Cell, *Expert Systems with Applications* **149** (2020), 113211. https://doi.org/10.1016/j.eswa.2020.113211.

[25] O. Ronneberger, P. Fischer and T. Brox, U-net: Convolutional networks for biomedical image segmentation (2015), In *International Conference on Medical image computing and computer-assisted intervention (pp. 234–241). Springer, Cham*. https://doi.org/10.1007/978-3-319-24574-4_28.

[26] K. Sanjar, O. Bekhzod, J. Kim, J. Kim, A. Paul and J. Kim, Improved U-Net: Fully Convolutional Network Model for Skin-Lesion Segmentation, *Applied Sciences* **10** (2020), 3658. https://doi.org/10.3390/app10103658.

[27] S. Graham, H. Chen, J. Gamper, Q. Dou, P.A. Heng, D. Snead and N. Rajpoot, MILD-Net: minimal information loss dilated network for gland instance segmentation in colon histology images, *Medical Image Analysis* **52** (2019), 199–211. https://doi.org/10.1016/j.media.2018.12.001.

[28] X. Xie, L. Li, S. Lian, S. Chen and Z. Luo, SERU: A cascaded SE-ResNeXT U-Net for kidney and tumor segmentation, *Concurrency and Computation: Practice and Experience* **32** (2020), e5738. https://doi.org/10.1002/cpe.5738.

[29] X. Hu and H. Yang, DRU-net: a novel U-net for biomedical image segmentation, *IET Image Processing* **14** (2019), 192–200. https://doi.org/10.1049/iet-ipr.2019.0025.

[30] X. Li, H. Chen, X. Qi, Q. Dou, C. W. Fu and P.A. Heng, H-DenseUNet: hybrid densely connected UNet for liver and tumor segmentation from CT volumes, *IEEE Transactions on Medical Imaging* **37** (2018), 2663–2674. https://doi.org/10.1109/TMI.2018.2845918.

[31] J. Park, J. Yun, N. Kim, B. Park, Y. Cho, H.J. Park and J.B. Seo, Fully automated lung lobe segmentation in volumetric chest CT with 3D U-net: validation with intra-and extra-datasets, *Journal of Digital Imaging* **33** (2020), 221–230. https://doi.org/10.1007/s10278-019-00223-1.

[32] F. Scotti, ALL-IDB, Acute Lymphoblastic Leukemia Image Database for Image Processing, In *2011 IEEE (pp. 2045–2048)*. https://doi.org/10.1109/ICIP.2011.6115881.

[33] M. Drozdzal, E. Vorontsov, G. Chartrand, S. Kadoury and C. Pal, The importance of skip connections in biomedical image segmentation, In *Deep Learning and Data Labeling for Medical Applications (2016), (pp. 179–187). Springer, Cham*. https://doi.org/10.1007/978-3-319-46976-8_19.

[34] Y. LeCun, Y. Bengio and G. Hinton, Deep learning (2015). nature 521. https://doi.org/10.1038/nature14539.

[35] T. Duan, Y. Tang, F. Gao and J. Yao, Application of mathematical morphology filter for noise reduction in photoacoustic imaging. In *Photons Plus Ultrasound: Imaging and Sensing*, **10878** (2019), 1087854. https://doi.org/10.1117/12.2512176.

[36] K. Hajian-Tilaki, Receiver operating characteristic (ROC) curve analysis for medical diagnostic test evaluation, *Caspian Journal of Internal Medicine* **4** (2013), 627. http://caspjim.com/article-1-193-en.html.

[37] F.H. Araujo, R.R. Silva, D.M. Ushizima, M.T. Rezende, C.M. Carneiro, A.G.C. Bianchi and F.N. Medeiros, Deep learning for cell image segmentation and ranking, *Computerized Medical Imaging and Graphics* **72** (2019), 13–21. https://doi.org/10.1016/j.compmedimag.2019.01.003.

[38] F. Long, Microscopy cell nuclei segmentation with enhanced U-Net, *BMC bioinformatics* **21** (2020), 1–12. https://doi.org/10.1186/s12859-019-3332-1.

[39] R. Hollandi, A. Szkalisity, T. Toth, E. Tasnadi, C. Molnar, B. Mathe and M. Kovacs, A deep learning framework for nucleus segmentation using image style transfer (2019). *bioRxiv*, 580605. http://dx.doi.org/10.1016/j.cels.2020.04.003.

[40] K. Sudha and P. Geetha, A novel approach for segmentation and counting of overlapped leukocytes in microscopic blood images, *Biocybernetics and Biomedical Engineering* (2020). https://doi.org/10.1016/j.bbe.2020.02.005.

[41] E.P. Mandyartha, F.T. Anggraeny, F. Muttaqin and F.A. Akbar, Global and Adaptive Thresholding Technique for White Blood Cell Image Segmentation (2020). In *Journal of Physics: Conference Series*. **1569** (2020), 022054. IOP Publishing. https://iopscience.iop.org/article/10.1088/1742-6596/1569/2/022054/pdf.